A Multifunctional Photoacoustic/Fluorescence Dual-Mode-Imaging Gold-Based Theranostic Nanoformulation without External Laser Limitations

Junfeng Zhang, Xiaofeng Yin, Chenchen Li, Xuelian Yin, Qianghua Xue, Lin Ding, Jiale Ju, Jifei Ma, Ying Zhu, Dongshu Du, Rui L. Reis, and Yanli Wang,*

Theranostics is a new type of biomedical technology that organically combines the diagnosis and therapy of diseases. Among molecular imaging techniques, the integration of photoacoustic (PA) and fluorescence (FL) imaging modes with high sensitivity and imaging depth provides precise diagnostic outcomes. Gold nanorods (Au NRs) are well-known contrast agents for PA imaging and photothermal therapy. However, their high toxicity, poor biocompatibility, rapid clearance, and the need for an external laser source limit their application. Therefore, modification of Au NRs with carbon-based nanomaterials (CBNs) is done to obtain a multifunctional dual-mode gold-based nanoformulation (mdGC), which preforms dual-mode imaging of PA and FL. The results show that mdGC promotes tumor cell apoptosis and exhibits good antitumor performance through the mitochondria-mediated apoptotic pathway by increasing the production of intracellular reactive oxygen species, reducing mitochondrial membrane potential, and regulating the expression of apoptosis-related genes. The targeting rate of mdGC to tumor tissue is up to $20.71 \pm 1.94\%$ ID g^{-1}; the tumor growth inhibition rate is as high as 80.44% without external laser sources. In general, mdGC is a potential multifunctional diagnostic and therapy integrated nanoformulation.

1. Introduction

Theranostics, which involves the integration of diagnosis and therapy in nanoformulations, is considered as the next genera-tion of personalized medicine to fulfill the challenges for accurate cancer diagnosis and effective therapy,[1] possessing benefits over a single diagnosis or therapy method. Theranostics for cancer have shown great potential in patient stratification and personalized medicine and real-time monitoring of nanodrug therapy processes, thus providing feedback regarding nanodrug therapy effects.[2] The diagnostic function of the theranostic system provides information about the location and size of the tumor in an organism, while the therapeutic function focuses on the antitumor effect of the drug.[3] Moreover, molecular imaging is the most advanced technology in medical imaging involved in tumor diagnosis, precision drug development, and other fields.[4] Among various techniques, photoacoustic (PA) imaging provides centimeter-level deep imaging depth, and fluorescence (FL) imaging has the advantage of having excellent resolution and sensitivity; hence it gained widespread attention. PA imaging is known to have low sensitivity, while FL imaging lacks spatial resolution; thus, the two possess their own strengths and weaknesses and have complementary benefits.

J. Zhang, C. Li, Y. Wang,
School of Pharmaceutical Sciences
Hainan University
Haikou 570228, P. R. China
E-mail: wangyanli@staff.shu.edu.cn

J. Zhang, X. Yin, C. Li, X. Yin, Q. Xue, J. Ju, R. L. Reis, Y. Wang,
Tumor Precision Targeting Research Center & Institute of Nanochemistry and Nanobiology
School of Environmental and Chemical Engineering
Shanghai University
Shanghai 200444, P. R. China

L. Ding
Translational Medicine Collaborative Innovation Center
The First Affiliated Hospital (Shenzhen People's Hospital)
Southern University of Science and Technology
Shenzhen 518055, P. R. China

J. Ma, Y. Zhu
Shanghai Institute of Applied Physics
Chinese Academy of Sciences
Shanghai 200444, P. R. China

D. Du
School of Life Sciences
Shanghai University
Shanghai 200444, P. R. China

R. L. Reis
3B's Research Group
I3Bs – Research Institute on Biomaterials Biodegradables and Biomimetics
University of Minho
Headquarters of the European Institute of Excellence on Tissue Engineering and Regenerative Medicine
Guimarães 4805-017, Portugal

**ADVANCED
SCIENCE NEWS**

www.advancedsciencenews.com

**ADVANCED
MATERIALS**

www.advmat.de

Therefore, the integration of PA and FL imaging modes having high sensitivity and imaging depth might achieve precise diagnostic outcomes.[5]

Gold nanorods (Au NRs) are well-known contrast agents for PA imaging and photothermal therapy due to their strong and broad absorption band in the near-infrared (NIR) region (600–900 nm) and high photothermal conversion efficiency.[6] Although a photosensitizer is designed and synthesized with high photothermal conversion efficiency, it still cannot overcome the disadvantages caused by external laser sources. First, high-power laser or repeated laser exposure may lead to adverse risks, such as occurrence of inflammatory disease and tumor metastasis.[7] Second, an NIR laser only produces an acceptable therapeutic effect on superficial tumors in the radiation area, with no effectiveness for metastatic tumors, possibly causing disease recurrence.[8] Third, hyperthermia induced by photothermal treatment is difficult to control. Laser power, exposure time, and focal spot size play an important role in the interaction of the laser with the tissue.[9] In addition, the theranostic applications of Au NRs are still limited by several disadvantages, such as toxicity of cetyltrimethylammonium bromide during the preparation of Au NRs, poor biocompatibility, and quick clearance after systematic administration.[10]

To overcome these shortcomings, we modified Au NRs with carbon-based nanomaterials (CBNs). CBNs, the synthesis of which was reported in our previous study, exhibit advantages of PA and FL imaging, nontoxicity, and good biocompatibility.[11] We have successfully prepared multifunctional dual-mode gold-based nanoformulations modified by CBNs (mdGC) and evaluated their performance in vitro and in vivo. Au NRs were used as the PA agent of mdGC due to their excellent PA imaging performance,[12] while CBNs were used as FL agent and PA enhancer of mdGC, owing to their better FL and PA imaging ability.

In this study, the potential of mdGC as an imaging contrast agent in PA and FL imaging was successfully demonstrated. mdGC was injected into mice through the tail vein, where the cumulative amount of Au at the tumor site reached 20.71% ID g^{-1} at 2 h and the tumor growth inhibition rate was as high as 80.44% without external laser sources, which greatly reduced the systemic side effects of Au NRs. Here, it has also been demonstrated to increase the production of intracellular reactive oxygen species (ROS), reduce mitochondrial membrane potential (MMP), regulate the expression of various factors (such as apoptosis-related genes p53, Caspase-3, and Apaf-1), increase the ratio of Bax/Bcl-2, and significantly reduce the expression of cell proliferation-related genes c-Myc and cyclin D1. We also showed that mdGC can increase the production of intracellular ROS and induce apoptosis of cancer cells free from the limitations of the external laser source for cancer therapy, and thus, was indicated to be a potential PA and FL imaging agent.

2. Results and Discussion

mdGC is a PA and FL imaging agent used to accurately diagnose and target tumor tissues to increase the production of intracellular ROS and induce apoptosis of cancer cells without the limitation of external laser sources.

2.1. Characteristics of Synthesized mdGC

Using the seedless method, by changing the reaction conditions[13] such as temperature,[14] ascorbic acid,[15] and NaBH$_4$, and pH,[16] Au NRs with a size of $(30 \pm 5.8) \times (9.2 \pm 1.2)$ nm were obtained in aqueous solution (**Figure 1**a,b and Figure S1, Supporting Information). As briefly noted earlier, CBNs were synthesized via a bottom-up method with an average diameter of 4.5 ± 1.5 nm (Figure 1c). The relevant characterizations[11] of CBNs are shown in Figure S2 (Supporting Information). To improve the biocompatibility of the Au NRs and reduce their toxicity, the CBNs (300 mg L^{-1}) were added to the Au NRs (300 mg L^{-1}) solution and stirred vigorously at 30 °C to obtain mdGC (Figures S1 and S3, and Table S1, Supporting Information).

2.2. Characteristics of Synthesized mdGC

TEM, UV–vis spectra, photoluminescence emission (PL) spectra, X-ray photoelectron spectroscopy, and zeta potential were used to verify the synthetic results. TEM revealed that the size of mdGC, which is $(33 \pm 3.6) \times (10.5 \pm 1.6)$ nm, is larger than that of Au NRs (Figure 1d,e). The UV–vis spectra of mdGC showed two broad peaks at 510 and 798 nm, while the Au NRs showed two broad peaks at 510 and 760 nm and CBNs at 372 nm (Figure 1f). In addition, fluorescence spectroscopy of CBNs exhibited an emission peak at 510 nm and mdGC that for appeared at 480 nm upon excitation at 373 nm, while Au NRs had no characteristic peak (Figure 1g). X-ray photoelectron spectroscopy showed that compared with Au NRs, the binding energy of mdGC did not shift, while changing only the intensity, which confirms that Au NRs and CBNs do not have chemical bonds between them (Figure 1h). As shown in **Table 1**, the zeta potential of mdGC decreased from primary 41.3 mV to –8.5 mV and the size increased from primary 40.4 to 191 nm in aqueous solution. The elemental mappings of the elements (S and Au) from the CBNs and Au NRs suggest an effective synthetic process for CBNs and Au NRs (Figure S4, Supporting Information). These results indicate that CBNs adsorbed around Au NRs by electrostatic force and successfully prepared a novel multifunctional nanoformulation, mdGC. In addition, mdGC has good stability in different media (in aqueous solution, in medium and in PBS) (Figure S5, Supporting Information).

To explore the PA performance of mdGC, we used a variable wavelength pulsed laser (680–970 nm) and an input laser with a power of 20 mJ cm^{-2}. The results show that mdGC exhibits stronger PA signal intensity than Au NRs (Figure 1i). This may be due to the PA enhancement effect of CBNs (Figure S6, Supporting Information), and the optimum laser wavelengths for mdGC and Au NRs were 720 and 730 nm, respectively (Figure 1j). In addition, we investigated the photoacoustic stability under continuous radiation generated by a pulsed laser (720 nm, 20 mJ cm^{-2}, 40 Hz repetitions, 5–7 ns laser pulses) for 5 min. The changes in the UV–vis spectra were monitored. After 5 min, the UV–vis spectra of mdGC remained basically unchanged, which is an indication of high photothermal stability under these conditions (Figure 1k,l).

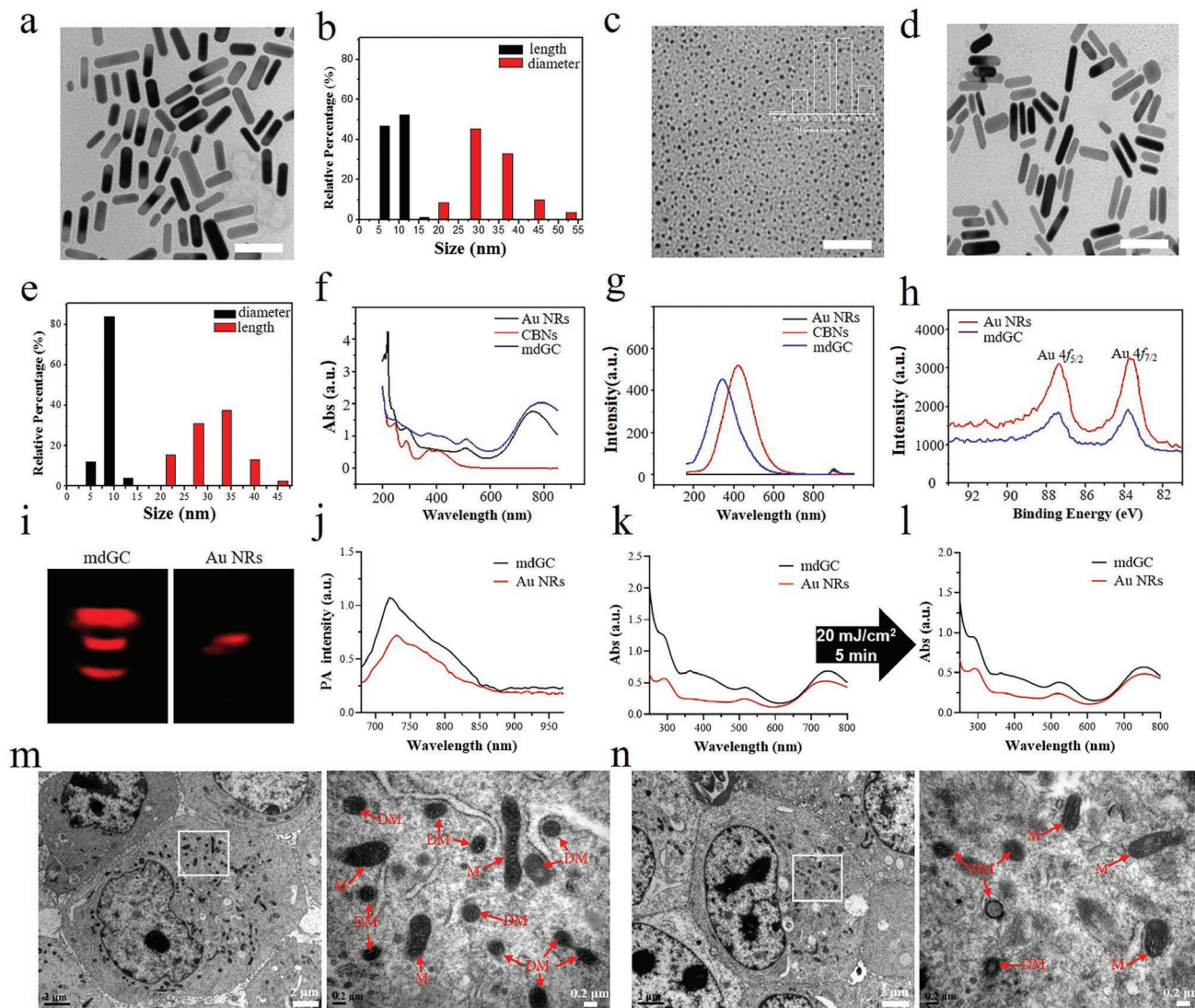Bio-TEM images showed that mdGC entered the 4T1 cells and reached the mitochondria. Compared with those of Au

Figure 1. Characteristics of synthesized materials. a,c,d) TEM images of Au NRs (a), CBNs (c), and mdGC (d). Scale bar: 50 nm. b,e) Particle size distribution of Au NRs (b), mdGC (e). f) UV–vis spectra of Au NRs, CBNs, and mdGC. g) PL spectra of Au NRs, CBNs and mdGC. h) X-ray photoelectron spectra of Au NRs and mdGC. i) Representative PA images obtained using excitation wavelengths of 720 nm of Au NRs and mdGC (input laser power: 20 mJ cm^{-2}; pulse rate: 40 Hz). j) Photoacoustic spectra of Au NRs and mdGC. k,l) UV–vis spectra of Au NRs and mdGC before (k) and after (l) laser illumination for 5 min (20 mJ cm^{-2}, 40 Hz). m,n) Bio-TEM images of 4T1 cells treated with mdGC (m) and Au NRs (n). M: mitochondrion; DM: damaged mitochondrion. The xperiment was repeated three times.

NRs-treated cells, most mitochondria showed reduced area and perimeter in mdGC-treated cells. Moreover, mitochondrial cristae almost completely disappeared in mdGC-treated cells. These results indicate that mdGC treatment disrupted mitochondrial morphology (Figure 1m,n).

2.3. In Vivo Antitumor Efficacy

In this study, in addition to demonstrating the potential of mdGC as an imaging contrast agent, we found that it increases the production of intracellular ROS, reduces MMP, regulates

Table 1. Zeta-potentials and hydrodynamic size of Au NRs, CBNs, and mdGC in aqueous solution, in medium, and in PBS.

	Zeta potential [mV]			Hydrodynamic size [nm]		
	In aqueous solution	In medium	In PBS	In aqueous solution	In medium	In PBS
Au NRs	41.3 ± 1.6	39.3 ± 2.4	40.5 ± 0.9	40.4 ± 2.2	38.4±3.3	39.9±1.8
CBNs	−28.5 ± 1.2	−25.2 ± 1.4	−29.8 ± 1.1	–	–	–
mdGC	−8.5 ± 0.6	−9.2 ± 0.5	−8.2 ± 0.3	191.3 ± 5.6	183.8 ± 2.7	198.8 ± 4.3

**ADVANCED
SCIENCE NEWS**

www.advancedsciencenews.com

**ADVANCED
MATERIALS**

www.advmat.de

the expression level of apoptosis-related genes, and participates in the induction of cell apoptosis through mitochondria-mediated pathways, without the need for external laser sources for cancer therapy (**Figure 2**a).

Au NRs and mdGC were intravenously injected into the tumor mice once every two days for 12 consecutive days to maintain an adequate dose in the tumor when the tumor volume of BALB/c mice reached 100 mm³. The results of the tumor relative volume curve showed that the tumor volumes in Au NRs and Au NRs + laser group decreased slightly as the tumor volumes in the saline group grew rapidly. However, the tumor volume was significantly reduced after 12 days of treatment with the mdGC without laser treatment, which was even smaller than that of the mdGC + laser group (Figure 2b). The tumor growth inhibition rate was calculated based on the relative tumor volume, where the four groups Au NRs, Au NRs + laser, mdGC, and mdGC + laser showed an inhibition rate of 27%, 38%, 69%, and 60%, respectively (Figure 2d). To further evaluate the therapeutic effect of mdGC, mice were sacrificed two days after the last intravenous injection and tumor tissues were collected. The tumor volume of the mdGC-treated group was the smallest among all the treated groups, and a significant difference between the mdGC and mdGC + laser groups was observed. The differences in tumor weight between the four groups also demonstrated excellent therapeutic efficiency (Figure 2e). In addition, during the whole treatment period, the weight of mice did not show apparent differences in any of the groups, which concludes that mdGC had no side effects on mice (Figure 2c).

In addition, we evaluated the antitumor effect of mdGC (300 mg L⁻¹) and Au NRs (300 mg L⁻¹) by administration via tail vein (continuous daily or every other day). The results showed that mice in the Au NRs group gradually revealed listlessness, anorexia, hair dullness, and other adverse reactions during administration every other day and began to die on day 14 after treatment, whereas the mdGC group mice exhibited a good condition (Figure 2g; Figure S7a, Supporting Information). In addition, the tumor growth inhibition rate of mdGC was as high as 80.44% according to the relative tumor volume (Figure 2f; Figure S7d, Supporting Information). The results were similar after daily administration. The Au NR group mice began to die on day 6 after treatment and the tumor growth inhibition rate of mdGC was as high as 78.49% (Figure S7b–e, Supporting Information). The above results prove that mdGC has excellent anticancer efficacy and no side effects in vivo.

2.4. Imaging Performance and Biodistribution

To evaluate imaging performance, mdGC and Au NRs (300 mg L⁻¹) were injected intravenously, PA imaging was performed at different time points (0.5, 2, 6, and 12 h), and tumor tissues were collected for fluorescence imaging.

It can be seen that the fluorescence signal of the tumor tissue is the highest at 2 h, indicating that mdGC can quickly reach the tumor tissue through blood circulation (**Figure 3**a,d). The results of PA imaging showed that mdGC had better PA imaging performance than Au NRs, with the highest photoacoustic signal at 2 h, which was consistent with the results of fluorescence imaging (Figure 3b,c,e).

To further study the in vivo biodistribution pattern of mdGC and Au NRs, BALB/c mice bearing tumors were intravenously injected with mdGC and Au NRs (300 mg L⁻¹). The mice were then sacrificed at 0.5, 2, 6, and 12 h after injection. Major organs and tissues (i.e., the heart, liver, spleen, lungs, kidney, brain, and tumor) were weighed and digested to determine the amount of Au using ICP-MS. The results showed that the accumulation of Au at the tumor site in the mdGC group was 20.71% ID g⁻¹ after 2 h of injection, while that in the Au NR group was only 3.78% ID g⁻¹ (Figure 3f,g). This result clearly indicates that mdGC has a higher targeting rate for tumor tissue, which is beneficial for imaging and therapy.

2.5. Biosafety and Toxicity In Vivo

The results of toxicity study of mdGC in vivo via intravenous injection demonstrated that mdGC had good biocompatibility and did not cause toxicity, even at high concentrations (300 mg L⁻¹). Blood was collected after 48 h of treatment and centrifuged at 3000 rpm for 5 min, and the upper serum was collected for biochemical analysis. Six parameters were used to evaluate in vivo toxicity: alanine aminotransferase, aspartate aminotransferase, alkaline phosphatase, lactic dehydrogenase, urea nitrogen, and serum creatinine. The results of the blood biochemical analysis exhibited a normal range compared to the control, indicating no damage to liver and kidney functions (**Figure 4**a). In addition, the results of hemolysis experiments showed that the hemolysis rates of mdGC at different concentrations (20, 40, 60, 80, and 100 mg L⁻¹) were all lower than 5%. It was reported that up to 5% hemolysis is permissible for biomaterials.[17] This shows that mdGC has good biosafety (Figure S8, Supporting Information). Histological analysis of the main organs further confirmed the low toxicity (Figure 4b). No clear signs of necrosis of the main organs were observed, including the heart, liver, spleen, lungs, kidney, and the brain. In addition, we calculated the organ coefficients of the mice (Figure S9, Supporting Information). Except for the spleen, other organs showed almost similar properties as those of the control group, implying that mdGC has low in vivo toxicity.

2.6. Endocytosis Mechanism and Cytotoxicity Study of mdGC

2.6.1. Endocytosis Mechanism Study of mdGC

To study the mechanism of endocytosis of mdGC, we first evaluated whether the endocytosis of mdGC was an energy-dependent process. Previous studies have shown that the available cell energy would significantly reduce at 4 °C.[18] The endocytosis amounts of mdGC were remarkably reduced by 4 °C incubation comparing with control group. In order to verify this result, we treated cells with NaN₃, which is known to inhibit the formation of ATP,[19] and got the same inhibitory effect. The results showed that endocytosis of mdGC was an energy-dependent process.

Endocytosis mechanisms of nanoparticles mainly have the following types: phagocytosis, macropinocytosis, clathrin, or caveolin-mediated endocytosis pathways.[20] Both phagocytosis
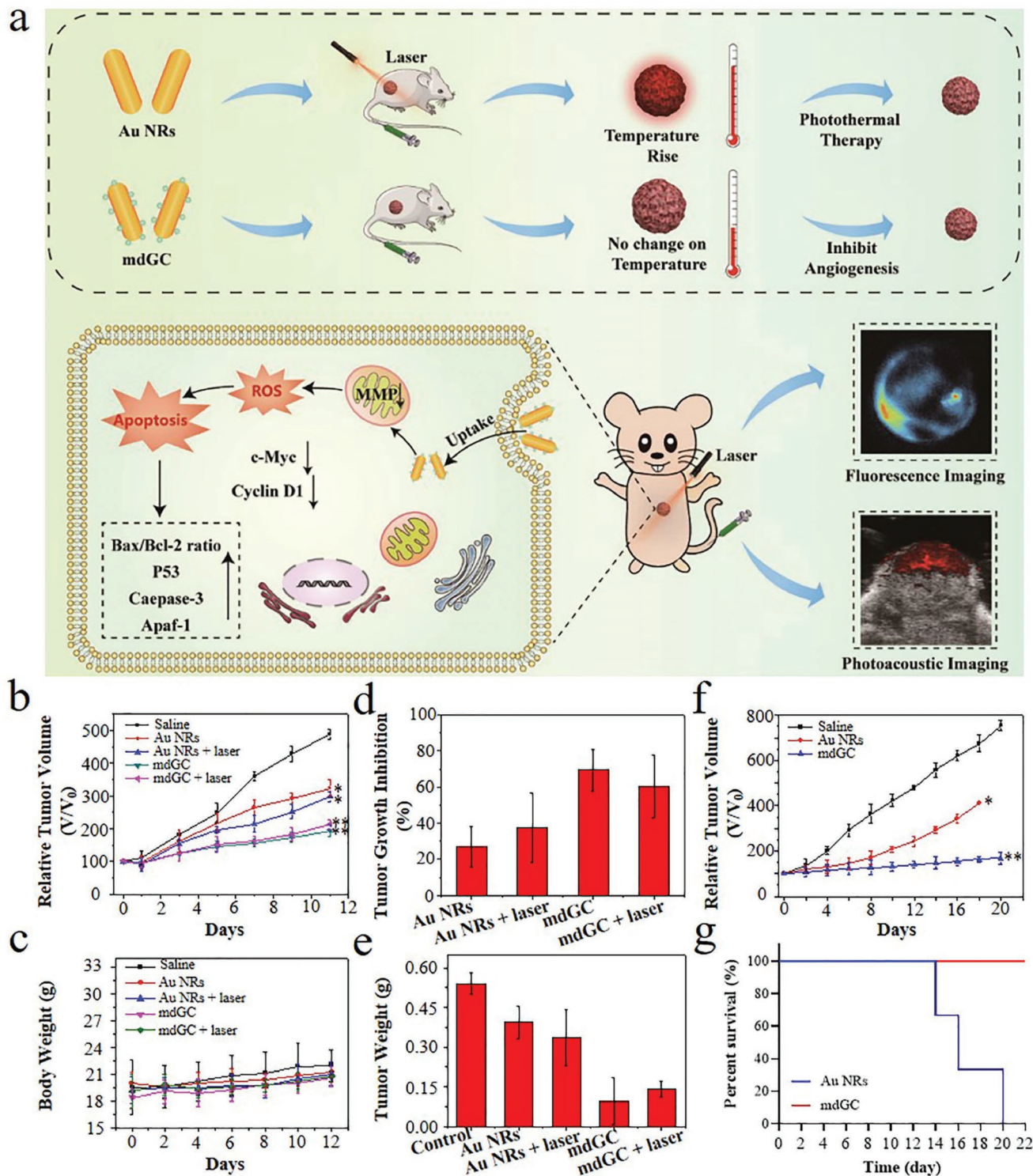
Figure 2. In vivo anticancer efficacy of mdGC. a) Schematic presentation of cancer therapy of mdGC. b) Relative tumor volume of mice after intravenously injected with saline and those in the Au NRs, Au NRs + laser, mdGC, mdGC + laser (300 mg L^{-1}, 808 nm, 5 W cm^{-2}, 5 min) groups ($n = 5$). c) Body weight changes of mice after intravenous injection in different treatment groups. d) Tumor inhibition rate on day 12 after receiving different treatments. e) The weight of tumor obtained from mice on day 12 after receiving different treatments. f) Relative tumor volume of mice after intravenous injection, every other day, with saline, Au NRs, and mdGC (300 mg L^{-1}) ($n = 5$). g) Percentage survival of mice after being intravenously injected with Au NRs and mdGC, administered every other day in two treatment groups. $^{**}P < 0.01$ and $^*P < 0.05$.

**ADVANCED
SCIENCE NEWS**

www.advancedsciencenews.com
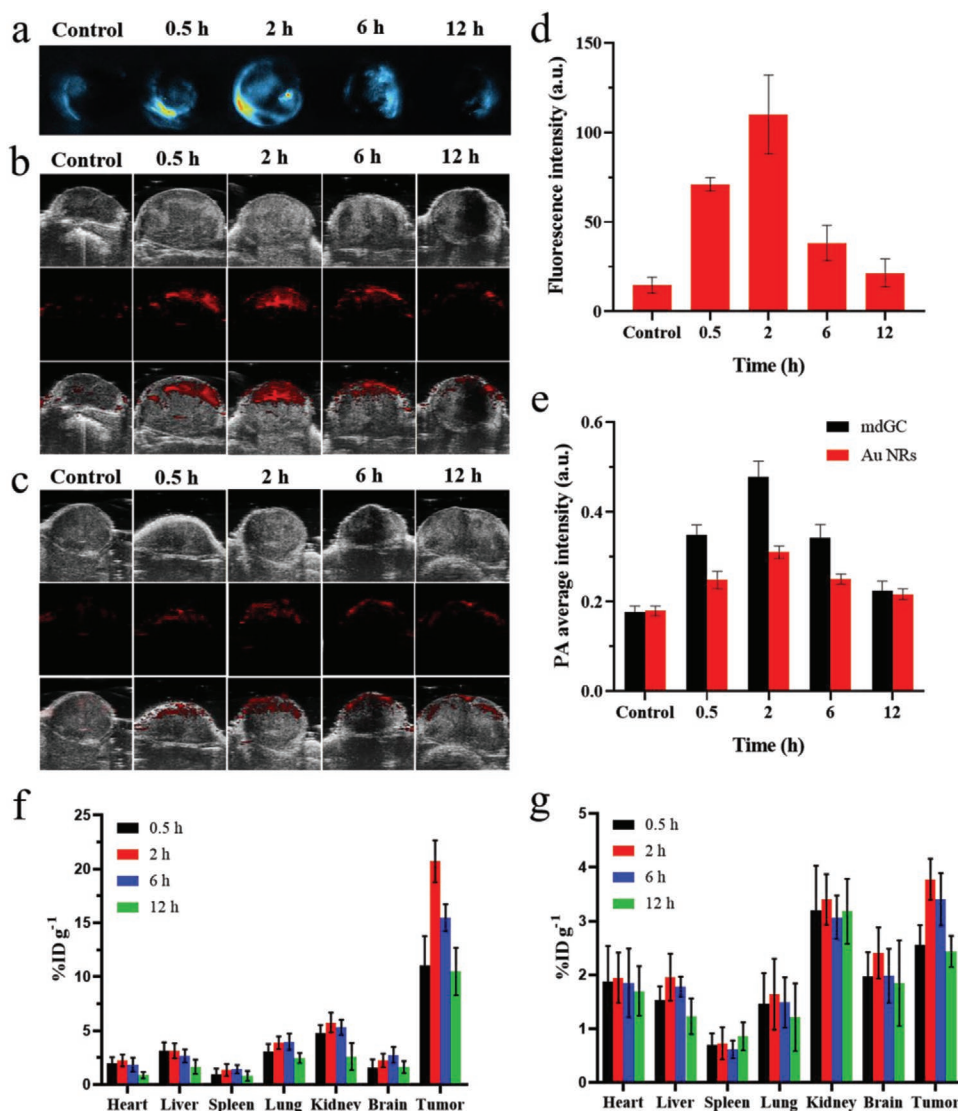
**ADVANCED
MATERIALS**

www.advmat.de

Figure 3. a) Fluorescence imaging of tumor tissue at different time points (0.5, 2, 6, and 12 h); the excitation wavelength was 405 nm. b,c) Photoacoustic imaging of tumor tissue using mdGC (b) and Au NRs (c) at different time points (0.5, 2, 6, and 12 h). d) Fluorescence signal of tumor tissue at different time points. e) Photoacoustic signal of tumor tissue at different time points. f,g) Biodistribution of mdGC (f) and Au NRs (g) in different organs at 0.5, 2, 6, and 12 h. Data are presented as mean ± standard deviation (SD), $n = 3$.

and macropinocytosis processes are dependent on actin-mediated remodeling of the plasma membrane at a large scale.[21] Clathrin-mediated endocytosis is the manner in which substance enters into the cells through the plasma membrane by clathrin coated vesicles. The vesicles are formed by contraction effect of dynamin and eventually shed from the plasma membrane.[22] Dynasore acts as a specific inhibitor of endocytic pathways that prevent the formation of dynamin.[23] We pretreated cells with chlorpromazine and dynasore to inhibit the formation of clathrin-coated vesicles and the dynamin-dependent endocytosis pathways, respectively.[24] The results showed that chlorpromazine pretreatment significantly inhibited mdGC internalization, while dynasore pretreatment did not. It indicates that the endocytosis of mdGC may be mediated by clathrin in principle, but not mediated by the endocytic pathway formed by dynamin. In conclusion, endocytosis of mdGC was an energy-dependent

process and was mediated by clathrin (Figure S10, Supporting Information).

2.6.2. Subcellular Location and Toxicity of mdGC In Vitro

A confocal laser microscope was used to observe the localization of mdGC in vitro. We found that CBNs cannot enter the cell, while mdGC can, owing to which it accumulated in the cytoplasm and mitochondria and enabled fluorescence imaging in vitro (**Figure 5**a; Figure S11, Supporting Information). However, the effect of time and laser irradiation on fluorescence imaging showed that the fluorescence intensity did not change significantly with time, while the cell morphology reformed slightly (Figure S12, Supporting Information), which was consistent with the results of the CCK-8 assay. No changes
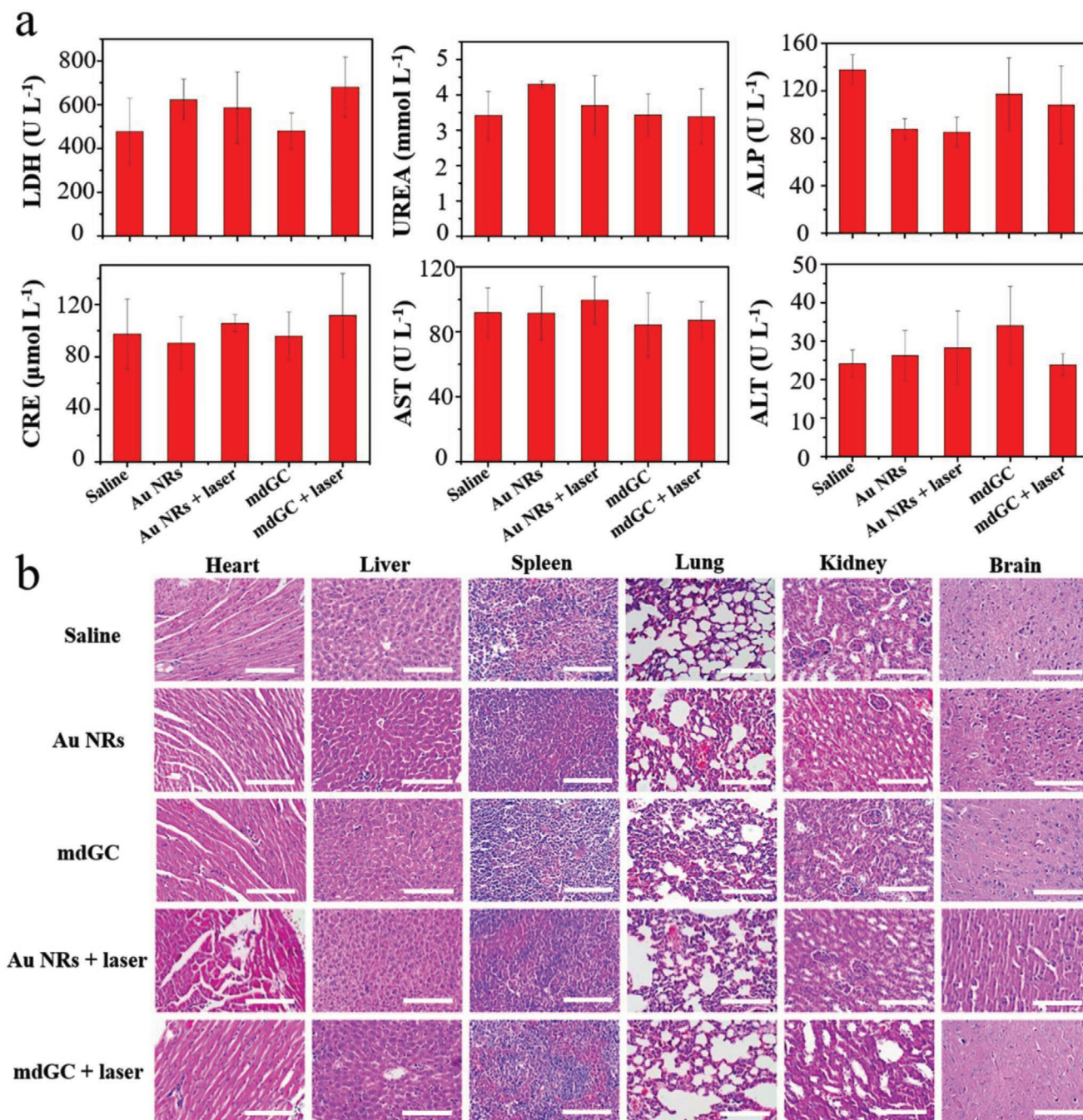
Figure 4. Biosafety and toxicity in vivo. a) Evaluation of serum biochemistry after different treatments via intravenous injections (300 mg L^{-1}, 808 nm, 5 W cm^{-2}, 5 min). b) Histological evaluation of toxicity of mdGC. Organs mainly include the heart, liver, spleen, lungs, kidney, and brain. ALT: alanine aminotransferase; AST: aspartate aminotransferase; ALP: alkaline phosphatase; LDH: lactic dehydrogenase; UREA: urea nitrogen; CRE: serum creatinine.

in fluorescence intensity were observed when exposed to laser irradiation, indicating that the mdGC has good stability and is an acceptable fluorescent imaging material.

The cytotoxicity of Au NRs and mdGC with and without laser irradiation was analyzed via the CCK-8 assay. The viability of 4T1 cells incubated with the mdGC for 12 h was lower, compared to those incubated with the Au NRs, which further decreased with laser exposure (808 nm, 5 W cm^{-2}, 3 min)

(Figure 5b). We then extended the incubation time to 24 and 48 h. The viability of cells incubated with the Au NRs with or without laser changed slightly, while that of cells incubated with mdGC with or without laser decreased significantly (Figure 5c,d). The results above showed that the toxicity of mdGC is higher than that of Au NRs at the same concentrations and their toxicity increased with an increase in exposure to laser irradiation. The human hepatoma cell line SMCC-7721
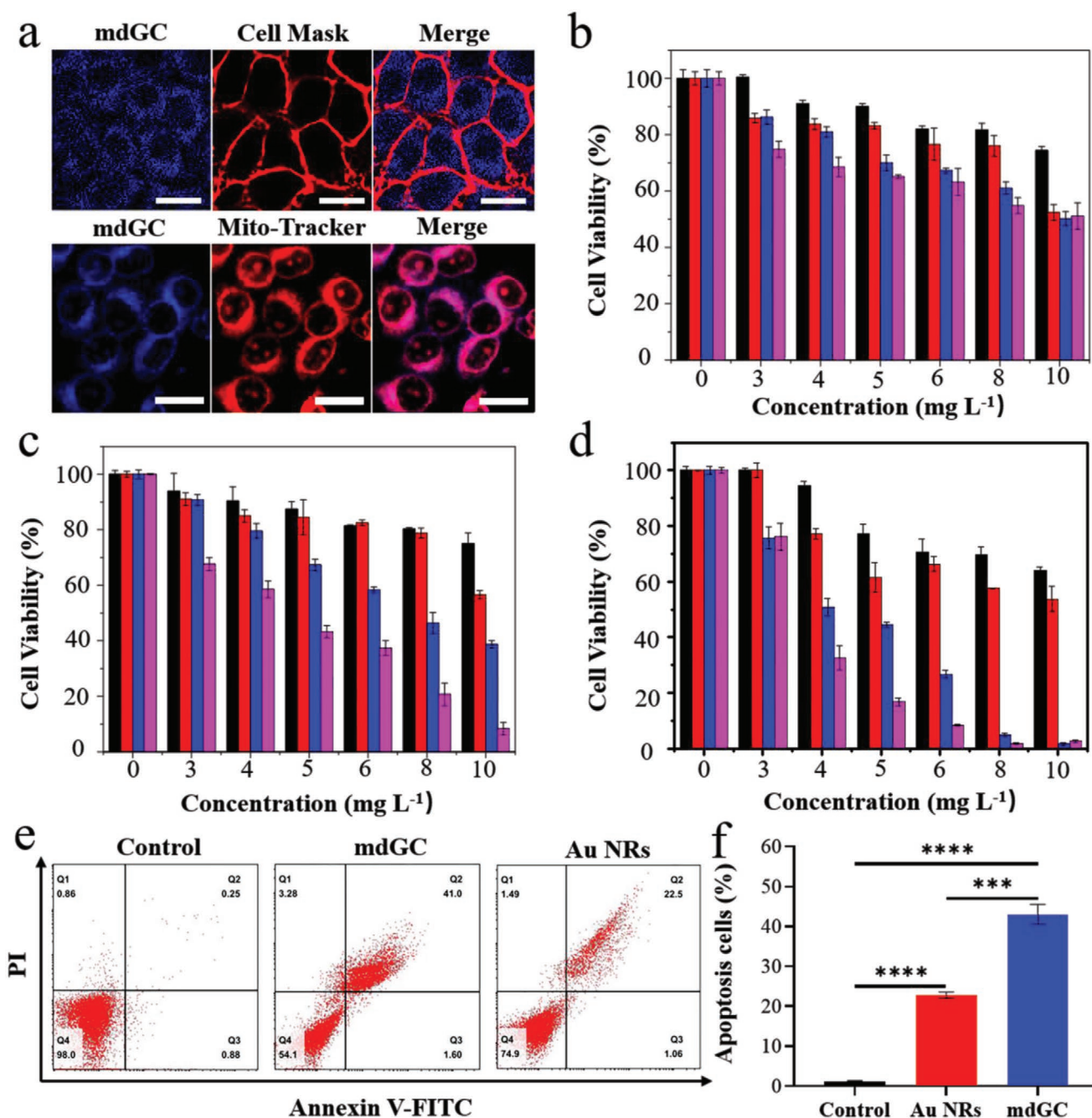
Figure 5. Toxicity of mdGC in vitro. a) Confocal microscopy image of mdGC in 4T1 cells. Scale bar: 20 μm. Cells were co-incubated with 3 mg L^{-1} mdGC for 2 h. b–d) Cytotoxicity of 4T1 cells incubated with the Au NRs and mdGC for different times at different concentrations: b) 12 h, c) 24 h, and d) 48 h. (The black color bar represents Au NRs group, the red color bar represents Au NRs + laser group, the blue color bar represents mdGC group, and the pink color bar represents mdGC + laser group). e) Analysis of the apoptosis of 4T1 cells after different treatments using Annexin V-FITC and PI staining apoptosis kit with flow cytometric analysis. f) Quantification of the percentage of apoptotic 4T1 cells after different treatments. $^{****}P < 0.0001$ and $^{***}P < 0.001$.

and human hepatocellular carcinoma cells (HepG2 cells) were used as research models (Figure S13, Supporting Information). The viability of SMCC-7721 cells was similar to that of 4T1 cells. However, in HepG2 cells, lower experimental doses could achieve similar toxicity.

Apoptosis refers to programmed cell death, which is a key mechanism used by antitumor drugs to control tumor growth.[25]

The effect of mdGC and Au NRs on 4T1 cell apoptosis was assessed via annexin V-FITC/PI staining and flow cytometry. The apoptosis rate of 4T1 cells with mdGC was 43.06 ± 2.47%, which was significantly higher than that of cells in the control group (1.24 ± 0.10%) and Au NR group (22.79 ± 0.77%), indicating that mdGC significantly increased the apoptosis of 4T1 cells (Figure 5e,f).

**ADVANCED
SCIENCE NEWS**

www.advancedsciencenews.com

**ADVANCED
MATERIALS**

www.advmat.de

2.7. Antitumor Mechanism of mdGC

2.7.1. The Antitumor Mechanism of mdGC does not Produce a Photothermal Effect

It is known that Au NRs irradiated with an external laser can convert light energy into heat energy, thus increasing the local temperature to kill the tumor cells. The temperature of cells in the Au NRs + laser (808 nm, 5 W cm^{-2}) group rose continuously with increasing laser irradiation time. However, the temperature of the group administered mdGC without the laser did not change (**Figure 6**a). This suggests that the mechanism by which mdGC inhibits tumor growth is not mediated by the photothermal effect. We further explored the temperature changes of different concentrations of mdGC with or without laser irradiation. The results

showed that the temperature of the mdGC + laser group cells increased with increasing mdGC concentration. However, the elevation in temperature was still too low to exert a photothermal effect to inhibit tumor growth (Figure 6b). However, when the laser was not used, the temperature did not change significantly with increasing concentration (Figure 6c). We also changed the power density (0.5–5 W cm^{-2}) of the laser and found that higher the laser power density, higher is the solution temperature (Figure 6d). This indicates that irrespective of the use of laser, the mechanism of killing tumor cells is different and is not associated with changes in temperature. We then explored the photothermal stability of mdGC (Figure 6e). The mdGC treatment was still able to increase the temperature to 40 °C after triplicate on/off irradiation cycles, which shows great photothermal stability and reusability. In contrast,
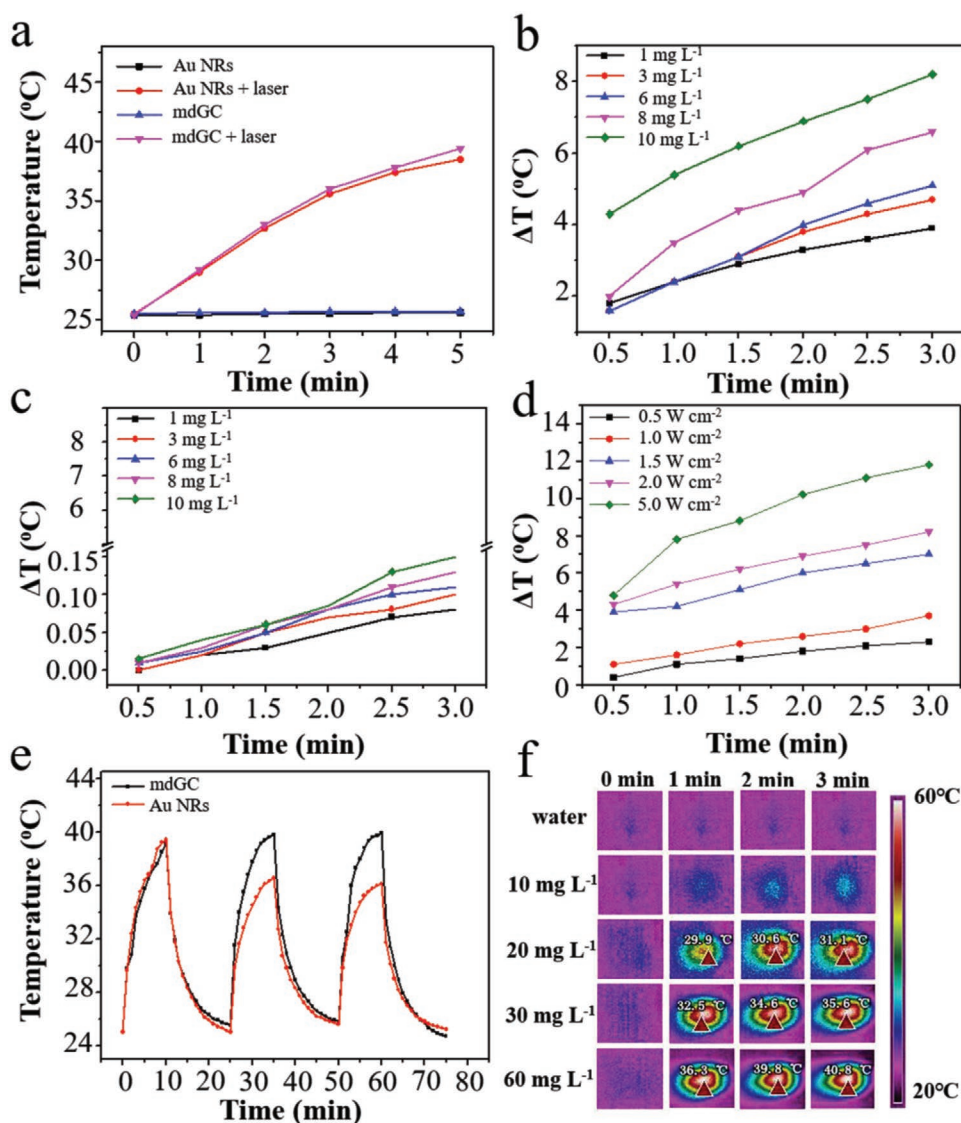

Figure 6. Evaluation of antitumor mechanism of mdGC. a) Change in temperature of Au NRs and mdGC with or without laser (808 nm, 5 W cm^{-2}) over 5 min. b,c) Temperature profiles for different concentrations of mdGC with laser (b) and without laser (c). d) Temperature profiles for different power densities of mdGC (20 mg L^{-1}). e) Temperature variations of mdGC and Au NRs (20 mg L^{-1}) under continuous irradiation with an 808 nm laser during triplicate cycles. f) Real-time thermal imaging for different concentrations of mdGC + laser.

ADVANCED
SCIENCE NEWS

www.advancedsciencenews.com

ADVANCED
MATERIALS

www.advmat.de

the laser irradiation stability of Au NRs is not as satisfactory, each irradiation reduces the peak temperature of the next irradiation. Consistently with previously reported results, Au NRs melt into Au nanospheres under prolonged or repeated 808 nm laser irradiation, and their photothermal conversion efficiency (PCE) decreases as the local surface plasmon resonance (LSPR) peak moves away from the wavelength of the laser.[26] After CBNs modified Au NRs, it can protect Au NRs and avoid that problem, so mdGC has better photothermal stability than Au NRs. We also recorded an image of real-time temperature change of mdGC using an infrared thermal imager, where the temperature of the mdGC kept rising under laser irradiation and rose to 42.7 °C in 5 min for 60 mg L^{-1} mdGC (Figure 6f). Thus, we can thus conclude that a temperature higher than 42 °C is theoretically sufficient to initiate a photothermal effect capable of killing tumor cells, whereas the inhibition of tumor growth may not be adequate if the temperature remains constant and does not rise to a higher level.

Currently, the mechanisms that have been reported to inhibit tumor growth include the following: 1) cancer cell death through apoptosis or necrosis,[27] 2) suppression of tumor growth via inhibition of angiogenesis to cut-off nutrition and oxygen supply to tumor cells,[28] and 3) increased aggregation of nanomaterials.[29] According to the results of previous studies and the above experimental data, we anticipate that mdGC induces cell apoptosis by regulating the expression of related gene proteins, thereby exerting antitumor effects. Therefore, we conducted experiments to explore the mechanism of cancer suppression.

2.7.2. Intracellular ROS Assay, MMP Assay, and Expression of Related Genes

Intracellular ROS Assay: Through interaction with proteins, ROS has an impact on several signaling pathways involved in the control of cell proliferation and apoptosis.[30] Here, we used the fluorescent probe DCFH-DA to detect the production of intracellular ROS. The results of confocal laser scanning microscopy (CLSM) fluorescence imaging clearly showed that green fluorescence was slightly detected in the control cells, which was significantly increased after treatment with mdGC and Au NRs (**Figure 7**a). Fluorescence semi-quantitative results further verified the production of intracellular ROS, where the ROS in mdGC group was much higher than that in the Au NRs group (Figure 7c), which was consistent with the results of quantitative detection of ROS production using Microplate System (λ_{ex} = 488 nm, λ_{em} = 525 nm) (Figure S14, Supporting Information). These results showed that since mdGC increased intracellular ROS levels, tumor cell apoptosis and inhibition of tumor growth was promoted.

Mitochondrial Membrane Potential (MMP) Assay: In many instances, mitochondria are crucial for the initiation of apoptosis, which is closely related to its dysfunction.[31] To explore the cytotoxic mechanism mediated by mdGC, we examined the changes in MMP in 4T1 cells treated with mdGC and Au NRs. The JC-1 probe is commonly used to measure the changes in MMP. In healthy cells with high MMP, JC-1 mainly forms an aggregate with red fluorescence. Since the mitochondrial function in injured cells is disturbed, leading to a decrease in MMP, its membrane is dominated by the green fluorescent JC-1 monomer. Fluorescence imaging results can be seen without any treatment in control cells exhibiting a strong red fluorescence; 4T1 cells after incubation with mdGC and Au NRs solution can lead to a significant reduction in red fluorescence and enhancement of green fluorescence intensity. The green fluorescence intensity in the cytoplasm of 4T1 cells incubated with Au NRs was significantly lower than that of cells incubated with mdGC (Figure 7b). Intracellular fluorescence changes may indicate a decrease in the accumulation of JC-1 aggregates in mitochondria and an increase in the diffusion of JC-1 molecules into the cytoplasm due to the increase in MMP with subsequent collapse of MMP. Fluorescence semi-quantitative results showed that the ratios of JC-1 aggregate/JC-1 monomer in the control, Au NRs, and mdGC groups were 51.95 ± 8.65, 24.65 ± 4.69, and 4.83 ± 1.78, respectively (Figure 7d). These data indicate that mdGC confers a greater damage to the mitochondria in the cells.

Expression of Related Genes: Excessive accumulation of ROS exceeds the homeostatic threshold, which is harmful to cells, further disrupting some physiological mechanisms such as proliferation, apoptosis, and angiogenesis.[32] The antiapoptotic mitochondrial protein Bcl-2 and the pro-apoptotic protein Bax are known to be vital regulators of programmed cell death. Many studies have shown that the Bax/Bcl-2 ratio determines the inhibitory effect of key factors on cell apoptosis. It is well known that apoptosis may lead to an increase in the production of ROS.[33] The p53 gene is a DNA replication regulator and a tumor suppressor gene that inhibits tumors by inducing apoptosis, and its inactivation leads to the reduction of apoptosis.[34] Caspase-3 activity is necessary for achieving hallmarks of apoptosis and is essential for processes related to cell rupture and apoptotic body formation.[35] c-Myc, a well-established oncogene, plays a vital role in the initiation and progression of various cancers.[36] Apoptotic protease activating factor-1 (Apaf-1) is an adaptor molecule that is crucial for activating initiator caspases and downstream effector caspases, which causes apoptosis directly.[37] Cyclin D1 has been recognized as a proto-oncogene and its overexpression can cause uncontrolled cell proliferation and malignancy. Cyclin D1 gene overexpression and gene amplification have been observed in a variety of tumors.[38] The results of this study showed that compared with the control group, the mdGC group showed a significantly upregulated expression of apoptosis-related genes p53, Caspase-3, and Apaf-1 and an increased ratio of Bax/Bcl-2. In addition, mdGC significantly reduced the expression of cell proliferation-related genes c-Myc and cyclin D1 (Figure 7e).

In general, we synthesized a multifunctional mdGC that can effectively ablate tumors without lasers. This is due to that mdGC can increase the production of intracellular ROS, decreases MMP, regulate the expression of apoptosis-related genes, and reduces the expression of cell proliferation-related genes c-Myc and cyclin D1 significantly. This indicates that the mitochondria-mediated pathway participates in the apoptosis induced by mdGC, thus exerting an antitumor effect.
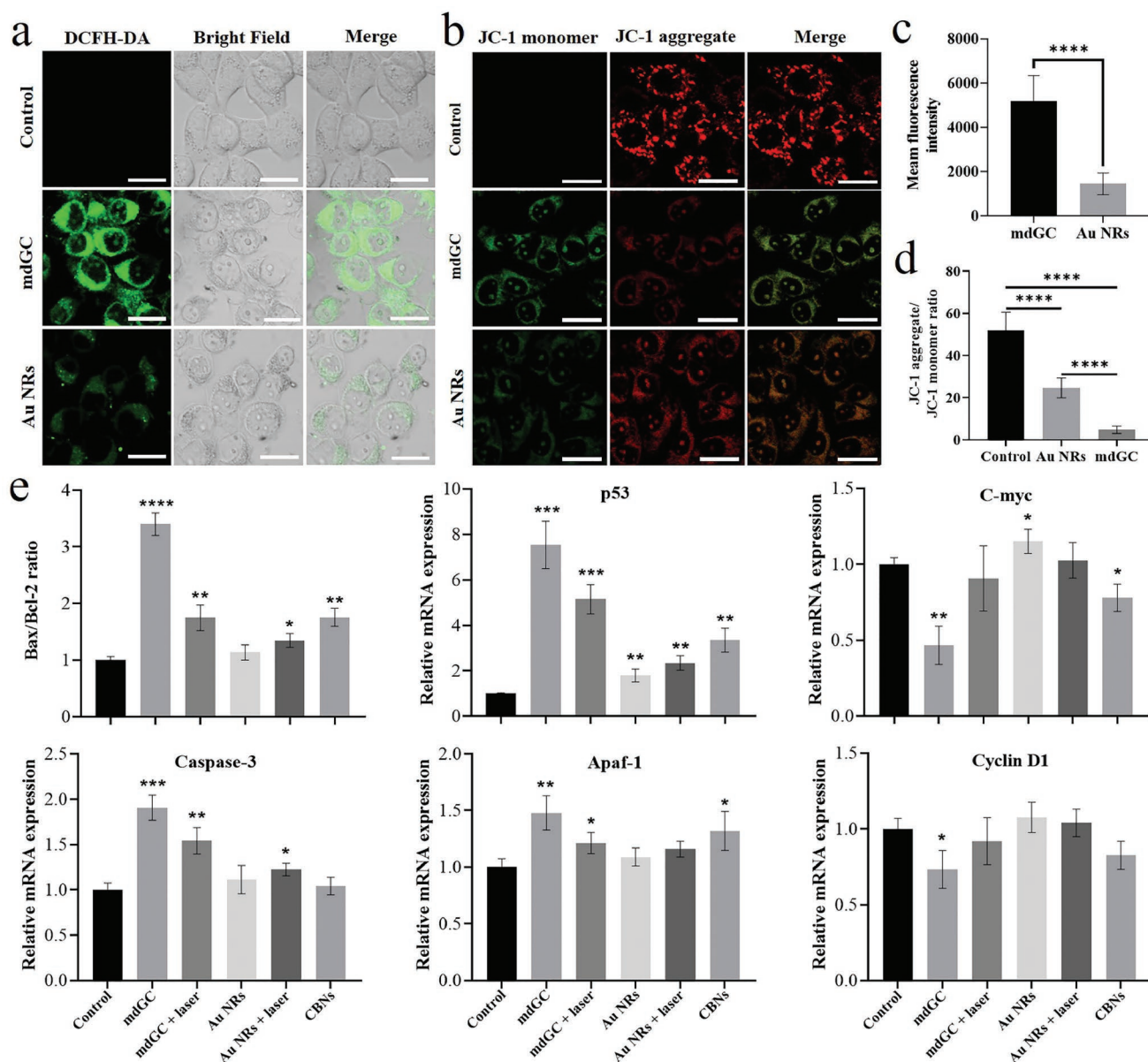
Figure 7. Study of the antitumor mechanism of mdGC. a) Fluorescence images of ROS produced after different treatments of 4T1 cells, as observed via CLSM. Scale bar: 20 μm. b) The JC-1 probe was used to stain 4T1 cells with different treatments, and the changes in cell mitochondrial membrane potential were observed via CLSM. c) The semi-quantitative fluorescence analyses of ROS produced by different treatments of 4T1 cells were performed using ImageJ software. d) Statistical analyses of the relative ratio of JC-1 aggregate/JC-1 monomer. e) Real-time PCR was used to quantitatively analyze the gene expression levels of Caspase-3, p53, Apaf-1, Bcl-2, Bax, c-Myc and Cyclin D1 in 4T1 cells that underwent different treatments. $****P < 0.0001$, $***P < 0.001$, $**P < 0.01$, and $*P < 0.05$.

3. Conclusion

We have successfully prepared mdGC, which exhibited potential for PA and FL imaging and eliminated the limitations that exist because of the use of external laser sources for cancer therapy. In vivo experiments showed that the targeting rate of mdGC to tumor tissue was up to $20.71 \pm 1.94\%$ ID g^{-1} after 2 h and the tumor growth inhibition rate was as high as 80.44% without external laser sources. Furthermore, mdGC increased the production of intracellular ROS; reduced MMP; regulated the expression of apoptosis-related genes p53, Caspase-3,

and Apaf-1; increased the ratio of Bax/Bcl-2; and significantly reduced the expression of cell proliferation-related genes c-Myc and cyclin D1. Our results showed that mdGC can participate in inducing cell apoptosis through mitochondria-mediated pathways without the need for external laser sources, thereby reducing the side effects of Au NRs, inhibiting tumor growth, and effectively overcoming heat problems caused by using a laser (e.g., the difficulty of controlling the hyperthermia process and high fever, which can lead to tumor migration).

In general, mdGC has been demonstrated to be a potential multifunctional diagnostic and therapy-integrated nanoformulation.

4. Experimental Section

Synthesis of Au NRs: Au NRs were synthesized using a seedless method. Cetyltrimethylammonium bromide (50.0 mL, 0.2 M) was added to 50 mL of chloroauric acid tetrahydrate (HAuCl$_4$·4H$_2$O) aqueous solution (0.2 M) under vigorous stirring at 30 °C, following which 2 mL of AgNO$_3$ (4.0 × 10^{-3} M) was added. Then, 120 μL of HCl (37%) was rapidly added to the solution to obtain a pH of ≈1.7, with subsequent addition of 750 μL of ascorbic acid (85.8 × 10^{-3} M) to the mixed solution. After the solution became clear, 75 μL of NaBH$_4$ (0.01 M) was immediately injected into the solution. After growing the nanorods for 6 h, the solution was washed to remove the unreacted ingredient via centrifugation three times at 12 000 rpm for 10 min.

Synthesis of mdGC: CBNs were synthesized based on a previously reported method.[11] mdGC was synthesized in ultrapure water via electrostatic adherence. The process was as follows: CBNs were added to an aqueous solution of gold nanorods under vigorous stirring at 30 °C, making it fully responsive for reaction. The final solution was purified with ultrapure water via three centrifugation cycles at 12 000 rpm for 10 min to remove unreacted materials.

Characterization: The shape and size were investigated using transmission electron microscopy (TEM, JEM-200CX, JEOL, Japan). UV–vis absorption and fluorescence spectra were recorded on a spectrophotometer (Hitachi 3100, Japan) and a fluorescence spectrophotometer (Hitachi 7000, Japan), respectively. The hydrodynamic size and zeta potential were measured using a Nano sizer (Zetasizer 3000 HS, Malvern, UK). The XPS spectra were recorded using an X-ray photoelectron spectrometer (Wscalab, English).

In Vitro Evaluation of PA Performance: Initially, a pulsed laser with variable wavelength (680–970 nm) and an input laser with a power of 20 mJ cm^{-2} were used. mdGC and Au NRs solutions were placed in NIR-inactive Tygon tubes (inner diameter, 0.127 cm). The PA signals detected by the linear array transducer (operating frequency, 13–24 MHz) were then used for the PA image reconstruction.

Subcellular Distribution: Bio-TEM was used to investigate the subcellular distribution of mdGC and Au NRs and the effect on the ultrastructure of cell organelles. 4T1 cells were incubated with mdGC (8 mg L^{-1}) and Au NRs (8 mg L^{-1}) in culture medium for 12 h. Next, 4T1 cells were fixed, sectioned (70 nm), and observed under TEM (HITACHI, HT7700).

Cell Culture: Mouse breast cancer cell line (4T1 cells), human hepatoma carcinoma cell line (SMMC-7721 cells), and hepatoma carcinoma cells (HepG2 cells) were purchased from the Chinese Academy of Sciences. Roswell Park Memorial Institute-1640 (RPMI 1640) cell culture medium, Dulbecco's modified Eagle's medium (DMEM), and fetal bovine serum (FBS) were purchased from Gino Biological Pharmaceutical Technology Co., Ltd. (Hangzhou, China). The cells were cultured in an appropriate culture medium (high-glucose RPMI 1640 for SMMC-7721, and DMEM for 4T1 and HepG2), supplemented with 10% FBS under a humidified 5% CO$_2$ and 95% air atmosphere at 37 °C.

Endocytosis Mechanism Study of mdGC: To study the endocytosis mechanism of mdGC, 4T1 cells (1.2 × 10^5 cells) were seeded in a confocal dish. After 24 h incubation, cells were treated with one of the following endocytosis inhibitor treatments for 0.5 h prior to the mdGC exposure: 1) incubated at 4 °C (instead of 37 °C); 2) addition of NaN$_3$ (10 × 10^{-3} M); 3) addition of dynasore (80 × 10^{-6} M); and 4) addition of chlorpromazine (50 × 10^{-6} M). Then the inhibitors were dumped and replaced with the medium containing mdGC (8 mg L^{-1}) for 1 h. The cells were then washed three times and observed using CLSM.

In Vitro Cytotoxicity: The cytotoxicity of mdGC was evaluated using the CCK-8 kit. Approximately, 5 × 10^3 4T1 cells, 5 × 10^3 SMMC-7721 cells, and 5 × 10^3 HepG2 cells per well were plated in 96-well plates. After incubation overnight, the medium was replaced and fresh medium containing Au NRs and mdGC was added to the plates at different time points (12, 24, and 48 h). The CCK-8 kit was then used to measure the viability of the cells in each well.

In Vitro Fluorescence Imaging of Cells: The 4T1 cells (1.2 × 10^5 cells) were seeded in a confocal dish, incubated overnight, and then treated with mdGC for different durations (1, 2, 4, 8, 12, and 24 h). Cells without any treatment were used as controls. After incubation, the cells were observed using CLSM.

Cell Apoptosis: Annexin V–FITC/PI Apoptosis Detection Kit (BD, USA) was used to analyze cell apoptosis. After culturing 4T1 cells with mdGC solution (8 mg L^{-1}) and Au NRs solution (8 mg L^{-1}) for 24 h, the cells were processed according to the manufacturer's protocol and analyzed via flow cytometry. Each experiment was performed in triplicate.

Intracellular ROS Detection: The DCFH-DA method was used to quantify intracellular ROS levels after 4T1 cell treatment. Briefly, 4T1 cells were cultured with mdGC solution (8 mg L^{-1}) and Au NRs solution (8 mg L^{-1}) for 24 h, and then, the ROS assay kit was used according to the manufacturer's instructions. The fluorescence of DCF was measured via CLSM and Microplate System to determine the generation of ROS.

Measurement of Mitochondrial Membrane Potential (MMP): The JC-1 probe was used to estimate changes in mitochondrial membrane potential. The cells were treated with mdGC solution (8 mg L^{-1}) and Au NRs solution (8 mg L^{-1}) for 24 h, incubated with JC-1 staining solution for 20 min and then immediately observed under CLSM. An excitation wavelength of 488 nm was selected for JC-1, and the emission wavelengths for JC-1 monomer and JC-1 aggregate were set to 515–545 and 570–600 nm, respectively.

Quantitative Real-Time PCR: This technique was used to quantify the expression levels of Bax, Bcl-2, p53, Caspase-3, c-Myc, Apaf-1, and Cyclin D1 genes. Total RNA was extracted from frozen tumor tissues using TRIzol reagent (Invitrogen, USA), following the manufacturer's instructions. For gene expression analysis, 2 μL of total RNA was reverse transcribed in a final volume of 20 μL to synthesize first-strand cDNA using the Revert Aid First Strand cDNA Synthesis Kit according to the manufacturer's instructions. Reverse transcription products (25 μL) were subjected to PCR in triplicate with an initial denaturation step of 95 °C for 10 min followed by 40 cycles, each consisting of 95 °C for 15 s, 60 °C for 60 s, followed by a dissolution curve from 75 to 95 °C and heating up by 1 °C every 20 s. The primer sequences used in this study are listed in **Table 2**.

In Vitro Fluorescence Imaging of Tumors: mdGC (300 mg L^{-1}) was intravenously injected into the mice via the caudal vein. Tumors were collected at predetermined time points (0.5, 2, 6, and 12 h), and analyzed in an in vivo imaging system (Cambridge Research & Instrumentation, Inc., USA) with an excitation wavelength of 405 nm for imaging.

In Vivo PA Imaging: PA imaging was performed using a small animal photoacoustic imaging system manufactured by Fujifilm VisualSonics Inc. (USA). A working laser wavelength of 720 nm was chosen with an average of 20 laser shots. Tumor-bearing mice were intravenously injected with mdGC or Au NRs (300 mg L^{-1}). The mice were anesthetized using an isoflurane–air mixture (2% isoflurane by volume) and placed in a horizontal position. PA imaging was performed at different time points (0.5, 2, 6, and 12 h).

ICP-MS Sample Preparation and Detection: mdGC (300 mg L^{-1}) and Au NRss (300 mg L^{-1}) were intravenously injected into the mice via the caudal vein. At predetermined time points (0.5, 2, 6, and 12 h), organs

Table 2. Primer sequences used for real-time PCR.

	Forward primer (5″-3″)	Reverse primer (5″-3″)
Bax	TTGCTACAGGGTTTCATCCAGG	GCAAAGTAGAAGAGGGCAACCA
Bcl-2	CTACCGTCGTGACTTCGCAGA	ACACATGACCCCACCGAAC
p53	CCCTCTGAGCCAGGAGACATTT	ACACTCGGAGGGCTTCACTTG
c-Myc	CCTTCTCTCCTTCCTCGGACT	TGCCTCTTCTCCACAGACACC
Caspase-3	TGGAAAGCC-GAAACTCTTCATCA	CCACGACCCGTCCTTTGAAT
Apaf-1	CAGATTCAGTA-ATGGGTCCTAAGC	TGAGGTAGTATGCCCAGCGAT
Cyclin D1	CGCCCTCCGTATCTTACTTCA	TCTTCGCACTTCTGCTCCTCA

such as the heart, liver, spleen, lungs, kidney, and brain, as well as tumors at the main organs of mice, were collected. All samples were completely digested in acid (3:1 mixture of HNO_3 and H_2O_2) on a hot plate prior to ICP analysis. The detection of gold content in samples treated with mdGC and Au NRss was performed using mass spectrometry (NexIon 300X, PerkinElmer).

Therapeutic Effect In Vivo: For in vivo therapy, female BALB/c mice (4 weeks) were purchased from the Shanghai Slack Experimental Animal Center (Shanghai, China). All animal experiments were performed following "the National Regulation of China for Care and Use of Laboratory Animals" and were approved by the Institutional Animal Care and Use Committee of Shanghai University.

Tumor-bearing mice were prepared by grafting 4T1 tumor pieces ($2 \times 2 \times 2$ mm^3 in size) into the right hind leg of the mice using a trocar. The mice were randomly divided into five groups when the tumor volume reached approximately 100 mm^3 ($n = 5$): a) saline control, b) Au NRss, c) Au NRss + laser (808 nm, 5 W cm^{-2}, 5 min), d) mdGC, and e) mdGC + laser (808 nm, 5 W cm^{-2}, 5 min). Au NRss and mdGC (100 μL each) were intravenously (0.3 mg mL^{-1}) injected. After 10 min, the tumor site was irradiated with 808 nm NIR irradiation for 5 min. After treatment, tumor size and body weight were measured every other day. Tumor volume was determined according to the following equation: $V_{tumor} = LW^2/2$ (L: tumor length, W: tumor width).

Evaluation of Toxicity In Vivo: For the in vivo toxicity evaluation, blood samples and major tissues were collected from mice after treatment. Serum was collected by centrifuging the blood at 3000 rpm for 5 min. Liver function was evaluated by assessing the serum levels of alanine aminotransferase, aspartate aminotransferase, alkaline phosphatase, and lactic dehydrogenase. Urea nitrogen and serum creatinine levels were assessed to evaluate nephrotoxicity. All biochemical parameters were determined according to the methods described in the references using commercial kits (Nanjing Jiancheng Bioeng Institute, China).

For hemolysis experiments, the mdGC immersed in saline for 24 h. Anticoagulated venous blood of healthy mice (0.2 mL) was added to each sample that has been equilibrated in saline for 30 min at 37 °C. After 10 min, 4 mL of PBS was added to each sample to stop the hemolysis and these samples were incubated for 60 min at 37 °C. Positive and negative controls were produced by adding 0.2 mL of venous blood to 4 mL of distilled water and saline, respectively. After incubation, the samples were centrifuged. The optical density of the supernatant was measured at 541 nm. The percentage of hemolysis was calculated as follows:

$$\%\text{hemolysis} = \left[\frac{(OD_{test} - OD_{neg})}{(OD_{pos} - OD_{neg})} \right] \times 100 \tag{1}$$

where OD_{test}, OD_{neg}, and OD_{pos} are the absorbance values of the test sample, negative control (saline) and positive control (water), respectively. Experiment was repeated three times.

All histological tests were performed using standard laboratory procedures. The tissues were fixed with 4% (v v^{-1}) formalin, embedded in a paraffin block, sectioned into 5 μm thickness, and then placed onto glass slides. After staining with H&E, the slides were examined by a pathologist using an optical microscope (Nikon U-III Multi Point Sensor System, USA).

Statistical Analysis: Data are expressed as the mean ± standard error of the mean (S.E.M.). Statistical analyses were performed using GraphPad Prism version 8. One-way analysis of variance (ANOVA) was used to compare the differences between the experimental groups, and Tukey's post hoc test was performed. *$P < 0.05$, **$P < 0.01$, ***$P < 0.001$, ****$P < 0.0001$ were considered significant.

Supporting Information

Supporting Information is available from the Wiley Online Library or from the author.

Conflict of Interest

The authors declare no conflict of interest.

Data Availability Statement

Research data are not shared.

[1] J. Zhou, L. Rao, G. C. Yu, T. R. Cook, X. Y. Chen, F. H. Huang, *Chem. Soc. Rev.* **2021**, *50*, 2839.

[2] N. Panwar, A. M. Soehartono, K. K. Chan, S. W. Zeng, G. X. Xu, J. L. Qu, P. Coquet, K. T. Yong, X. Y. Chen, *Chem. Rev.* **2019**, *119*, 9559.

[3] J. J. Du, N. Xu, J. L. Fan, W. Sun, X. J. Peng, *Small* **2019**, *15*, 1805087.

[4] M. Gao, F. B. Yu, C. J. Lv, J. Choo, L. X. Chen, *Chem. Soc. Rev.* **2017**, *46*, 2237.

[5] a) J. C. Ge, Q. Y. Jia, W. M. Liu, L. Guo, Q. Y. Liu, M. H. Lan, H. Y. Zhang, X. M. Meng, P. F. Wang, *Adv. Mater.* **2015**, *27*, 4169; b) J. Qi, C. Chen, X. Y. Zhang, X. L. Hu, S. L. Ji, R. T. K. Kwok, J. W. Y. Lam, D. Ding, B. Z. Tang, *Nat. Commun.* **2018**, *9*, 1848.

[6] J. B. Qin, Z. Y. Peng, B. Li, K. C. Ye, Y. X. Zhang, F. K. Yuan, X. R. Yang, L. J. Huang, J. Q. Hu, X. W. Lu, *Nanoscale* **2015**, *7*, 13991.

[7] W. H. Chen, G. F. Luo, Q. Lei, S. Hong, W. X. Qiu, L. H. Liu, S. X. Cheng, X. Z. Zhang, *ACS Nano* **2017**, *11*, 1419.

[8] J. Nam, S. Son, L. J. Ochyl, R. Kuai, A. Schwendeman, J. J. Moon, *Nat. Commun.* **2018**, *9*, 1074.

[9] a) J. Q. Chen, C. Y. Ning, Z. N. Zhou, P. Yu, Y. Zhu, G. X. Tan, C. B. Mao, *Prog. Mater. Sci.* **2019**, *99*, 1; b) A. Bucharskaya, G. Maslyakova, G. Terentyuk, A. Yakunin, Y. Avetisyan, O. Bibikova, E. Tuchina, B. Khlebtsov, N. Khlebtsov, V. Tuchin, *Int. J. Mol. Sci.* **2016**, *17*, 1295.

[10] S. W. Liu, L. Wang, M. Lin, D. D. Wang, Z. Q. Song, S. Y. Li, R. Ge, X. Zhang, Y. Liu, Z. M. Li, H. C. Sun, B. Yang, H. Zhang, *ACS Appl. Mater. Interfaces* **2017**, *9*, 44293.

[11] a) Z. D. Lei, L. Ding, C. J. Yao, F. F. Mo, C. C. Li, Y. N. Huang, X. L. Yin, M. Li, J. L. Liu, Y. Zhang, C. Q. Ling, Y. L. Wang, *Adv. Mater.* **2019**, *31*, 1807456; b) J. F. Zhang, C. C. Li, Q. H. Xue, X. L. Yin, Y. J. Li, W. He, X. R. Chen, J. Zhang, R. L. Reis, Y. L. Wang, *Small Methods* **2021**, *5*, 2100539.

[12] J. Weber, P. C. Beard, S. E. Bohndiek, *Nat. Methods* **2016**, *13*, 639.

[13] B. N. Khlebtsov, V. A. Khanadeev, J. Ye, G. B. Sukhorukov, N. G. Khlebtsov, *Langmuir* **2014**, *30*, 1696.

ADVANCED
SCIENCE NEWS

www.advancedsciencenews.com

ADVANCED
MATERIALS

www.advmat.de

[14] P. Zijlstra, C. Bullen, J. W. M. Chon, M. Gu, *J. Phys. Chem. B* **2006**, *110*, 19315.

[15] H. H. Chang, C. J. Murphy, *Chem. Mater.* **2018**, *30*, 1427.

[16] a) A. K. Samal, T. S. Sreeprasad, T. Pradeep, *J. Nanopart. Res.* **2009**, *12*, 1777; b) M. R. K. Ali, B. Snyder, M. A. El-Sayed, *Langmuir* **2012**, *28*, 9807.

[17] A. Datta, S. Dasgupta, S. Mukherjee, *J. Nanopart. Res.* **2017**, *19*, 142.

[18] L. Ding, C. J. Yao, X. F. Yin, C. C. Li, Y. N. Huang, M. Wu, B. Wang, X. Y. Guo, Y. L. Wang, M. H. Wu, *Small* **2018**, *14*, 1801451.

[19] a) C. Brandenberger, C. Mühlfeld, Z. Ali, A. G. Lenz, O. Schmid, W. J. Parak, P. Gehr, B. Rothen-Rutishauser, *Small* **2010**, *6*, 1669; b) B. D. Chithrani, W. C. W. Chan, *Nano Lett.* **2007**, *7*, 1542.

[20] H. Gao, W. Shi, L. B. Freund, *Proc. Natl. Acad. Sci. USA* **2005**, *102*, 9469.

[21] S. Mayor, R. E. Pagano, *Nat. Rev. Mol. Cell Biol.* **2007**, *8*, 603.

[22] H. T. McMahon, E. Boucrot, *Nat. Rev. Mol. Cell Biol.* **2011**, *12*, 517.

[23] E. Macia, M. Ehrlich, R. Massol, E. Boucrot, C. Brunner, T. Kirchhausen, *Dev. Cell* **2006**, *10*, 839.

[24] J. Rejman, A. Bragonzi, M. Conese, *Mol. Ther.* **2005**, *12*, 468.

[25] E. Obeng, *Braz. J. Biol.* **2021**, *81*, 1133.

[26] a) Y. J. Liu, B. Pravin, Z. F. Dai, X. Y. Chen, *Chem. Soc. Rev.* **2019**, *48*, 2053; b) G. L. Fu, W. Liu, S. S. Feng, X. L. Yue, *Chem. Commun.* **2012**, *48*, 11567; c) S. Link, C. Burda, M. B. Mohamed, B. Nikoobakht, M. A. El-Sayed, *J. Phys. Chem. A* **1999**, *103*, 1165.

[27] Z. B. Li, H. Huang, S. Y. Tang, Y. Li, X. F. Yu, H. Y. Wang, P. H. Li, Z. B. Sun, H. Zhang, C. L. Liu, P. K. Chu, *Biomaterials* **2016**, *74*, 144.

[28] a) N. H. Goradel, F. Ghiyami-Hour, S. Jahangiri, B. Negahdari, A. Sahebkar, A. Masoudifar, H. Mirzaei, *J. Cell. Physiol.* **2018**, *233*, 2902; b) R. L. Longoria, M. C. Cox, W. D. Figg, *Clin. Genitourin. Cancer* **2005**, *4*, 197; c) C. Hwang, E. I. Heath, *J. Hematol. Oncol.* **2010**, *3*, 26.

[29] Q. F. Ban, T. Bai, X. Duan, J. Kong, *Biomater. Sci.* **2017**, *5*, 190.

[30] B. Perillo, M. Di Donato, A. Pezone, E. Di Zazzo, P. Giovannelli, G. Galasso, G. Castoria, A. Migliaccio, *Exp. Mol. Med.* **2020**, *52*, 192.

[31] F. J. Bock, S. W. G. Tait, *Nat. Rev. Mol. Cell. Biol.* **2020**, *21*, 85.

[32] S. H. Ebadollahi, M. Pouramir, E. Zabihi, M. Golpour, M. Aghajanpour-Mir, *Cell J.* **2021**, *22*, 532.

[33] L. L. Jing, J. Shao, W. Sun, T. Lan, Z. P. Jia, H. P. Ma, H. B. Wang, *Life Sci.* **2020**, *248*, 116481.

[34] M. Salarkarmi, B. Shahouzehi, S. Rahemi, H. Fallah, *Biointerface Res. Appl. Chem.* **2020**, *11*, 9157.

[35] N. Pilco-Ferreto, G. M. Calaf, *Int. J. Oncol.* **2016**, *49*, 753.

[36] J. C. Ge, W. D. Yu, J. H. Li, H. B. Ma, P. Y. Wang, Y. H. Zhou, Y. Wang, J. Zhang, G. W. Shi, *J. Exp. Clin. Cancer Res.* **2021**, *40*, 59.

[37] H. H. Ma, X. M. Yan, L. Yan, J. Y. Zhao, J. P. Song, R. Peng, Y. B. Yang, J. X. Peng, K. Y. Liu, *Insects* **2021**, *12*, 64.

[38] S. Qie, J. A. Diehl, *J. Mol. Med.* **2016**, *94*, 1313.

2110690 (14 of 14)